

Experimental Velocity Fields Evaluation under the Rotor/Propeller Interactions for High Speed Helicopters for Different Propeller Positions

Lauriane LEFEVRE (✉ lauriane.lefevre@onera.fr)

Office National d'Études et de Recherches Aérospatiales

Vianney NOWINSKI

Office National d'Études et de Recherches Aérospatiales

Jerome DELVA

Univ. Lille, CNRS, ONERA, Arts et Métiers Institute of Technology, Centrale Lille, UMR 9014-LMFL-
Laboratoire de Mécanique des Fluides de Lille - Kampé de Fériet

Antoine DAZIN

Univ. Lille, CNRS, ONERA, Arts et Métiers Institute of Technology, Centrale Lille, UMR 9014-LMFL-
Laboratoire de Mécanique des Fluides de Lille - Kampé de Fériet

Research Article

Keywords:

Posted Date: June 22nd, 2022

DOI: <https://doi.org/10.21203/rs.3.rs-1753067/v1>

License:  This work is licensed under a Creative Commons Attribution 4.0 International License.

[Read Full License](#)

Experimental Velocity Fields Evaluation under the Rotor/Propeller Interactions for High Speed Helicopters for Different Propeller Positions

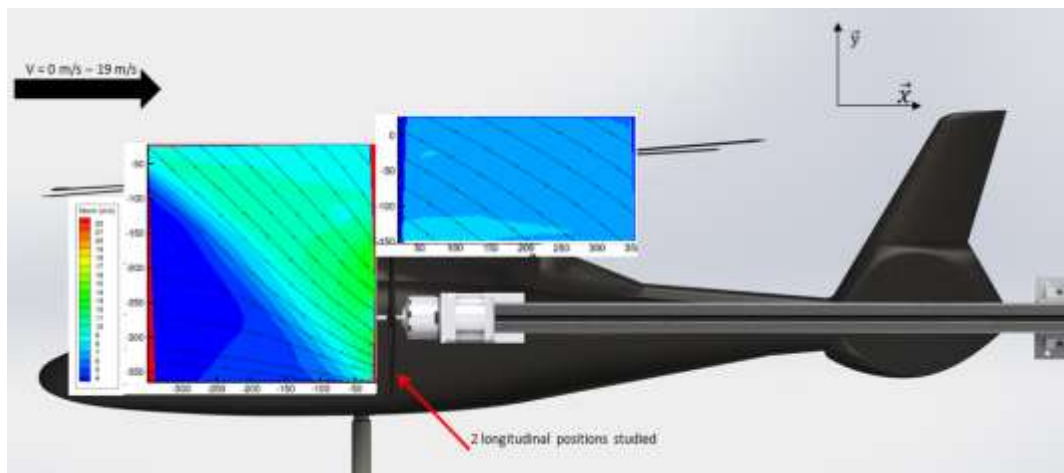
	Lauriane LEFEVRE ⁽¹⁾ <i>Ph.D Candidate,</i> <i>ONERA</i>	
Vianney NOWINSKI ⁽¹⁾ <i>Doctor,</i> <i>ONERA</i>	Jérôme DELVA ⁽¹⁾ <i>ONERA</i>	Antoine DAZIN ⁽¹⁾ <i>Professor,</i> <i>ENSAM</i>

(1) Univ. Lille, CNRS, ONERA, Arts et Métiers Institute of Technology, Centrale Lille, UMR 9014-LMFL- Laboratoire de Mécanique des Fluides de Lille - Kampé de Fériet, F-59000, Lille, France.

Abstract

This paper focuses on the experimental evaluation of the rotor/propeller interactions for hybrid compound configurations. Experiments are conducted in the ONERA L2 large size-low speed wind tunnel with a 1/7.7 Dauphin 365N model and a four-bladed small-scale propeller. PIV measurements are performed to visualize the velocity fields around the helicopter. Different flight conditions (wind speeds, and propeller position) are tested.

In hover, the propeller is completely immersed in the rotor wake for all the configurations, and the thrust is therefore maximal. At low speed, the propeller is partially immersed and the flow on the propeller disk is highly asymmetrical. In this flight configuration, moving the propeller towards the tail of the device increases the interactions and thus the performances of the propeller. No direct interactions of the two rotating parts are measured at high speed for all the configurations tested.



Nomenclature

b	Number of rotor blades
c	Blade chord (m)
F_z	Thrust (N)
R_{prop}	Propeller radius (m)
R_{rotor}	Rotor radius (m)
S	Rotor disk surface (m ²)
V	Free stream velocity (m/s)
V_{tip}	Blade tip rotation velocity (m/s)
\bar{Z}	Thrust coefficient ($\bar{Z} = \frac{100 \cdot F_z}{\frac{1}{2} \rho S \sigma (R\Omega)^2}$)
α	Flow angle ($\alpha = \arctan(V / U)$, °)
μ	Advance ratio ($\mu = V / V_{tip}$)
ρ	Air density (kg/m ³)
σ	Rotor solidity ($\sigma = \frac{b c}{\pi R_{rotor}}$)
Ω_{prop}	Propeller rotational velocity (rpm)
Ω_{rotor}	Rotor rotational velocity (rpm)

Introduction

Helicopters are widely recognized for their hovering and vertical take-off and landing (VTOL) capabilities. While the demand has increased due to the multiplication of air transport, classical configurations present limitations such as a maximum speed limited to around 300 km/h. At high speed, conventional gyroplanes can indeed undergo compressibility issues on the advancing blade and negative lift on the retreating side of the main rotor. This restricted speed limits the adaptability of the helicopters to a wider range of missions.

In this context, the compound helicopters have been designed to increase the maximal reachable speed. Including additional lift wings and/or rotors, these setups lead to a rotor slow-down allowing the device to reach higher speeds while maintaining a minimal rotor drag. Multiple configurations have been thought out: the tail propeller, the lift wing, the tilt rotor, the tandem, or the coaxial compound helicopter. Amongst the

compound configurations, the hybrid helicopter is equipped with two side propellers mounted on a lift-wing. Two examples are the Eurocopter X3 that reached the velocity of 472 km/h in 2014, and the Airbus Helicopters RACER that is optimized for a cruise speed of 400km/h (Figure 1). In this configuration, the propellers have two key functions: 1) providing thrust to increase the maximum speed, and 2) creating an efficient anti-torque to preserve the hovering abilities.



Fig. 1 - Eurocopter X3 (left) and Airbus Helicopters RACER (right)

However, the multiplication of rotating elements leads to complex and important interactions. Numerical studies have been conducted on the rotor/wing (Orchard and Newman 2003; Floros and Johnson 2009; Ferguson and Thomson 2015; Lorber et al. 2016; Öhrle et al. 2021), rotor/fuselage (Rand and Khromov 2015; Russell and Johnson 2012), wing/propeller (Thiemeier et al. 2019), and rotor/propeller interactions (Yeo and Johnson 2007), but very few experimental research is available to date (Stokkermans 2020; Lefevre et al. 2021). In this context, this paper experimentally evaluates the aerodynamic rotor/propeller interactions for the hybrid compound helicopter in different flight configurations.

More precisely, the objective of this study is to estimate the influence of the position of the propeller on the interactions between the rotating elements for different flight configurations.

To do so, velocity fields are measured using PIV. Experiments took place in the ONERA L2 large size-low speed wind tunnel with a small-scale DAUPHIN 365N model and a four-bladed propeller.

This paper analyzes velocity fields at low ($\mu = 0.06$) and high speeds ($\mu = 0.22$). Measurements are realized for a relative position of the propeller to the helicopter similar to the Eurocopter X3 ($x = 0.14$ m upstream of the rotor head), and in a configuration where the propeller is aligned with the rotor center. The influence of the advance ratio on the rotor/propeller interactions is presented for each configuration.

A previous study detailed the behavior of the flow in the nominal position for different advance ratios (Lefevre et al. 2022).

Experimental setup

The main rotor

A 1/7.7 scale DAUPHIN 365N helicopter made of glass fiber has been used for this study (Figure 2). This model has been characterized at ONERA since its manufacturing in the 1980's (Le Pape A., Gatard J., and Monnier J.-C. 2007; Renaud et al. 2008). The small-scale helicopter is 1.467 m long and 0.417 m high. The rotor is fully articulated and equipped with four glass-filled nylon rectangular blades with the following characteristics: blade section OA209, a chord of 0.05 m, linear twist angle of $-16^\circ/\text{m}$. The rotor diameter is 1.5 m and the head is tilted 4° towards the nose of the device.

The thrust coefficient is the same as the full-scale helicopter ($\bar{Z} = 14.5$ to represent a moderate loading). The main rotor nominal rotational speed is 1100 rpm, which corresponds to a blade tip speed of 86 m/s. The setting accuracy is of ± 10 rpm, and the measurement uncertainty is less than 50 rpm. The propeller is placed under the advancing blade, on the port side of the helicopter.

As for a full-size helicopter, the collective and cyclic pitch angles are controllable and measurable. The blade pitch, flap and lead-lag angles are also monitored. An air-cooling circuit is installed to limit the motor heating during the measurements.

To ensure the safety of the device, the rotational speed of the main rotor has been chosen to avoid the resonance frequencies.



Figure 2 - Installation of the full assembly in the L2 wind tunnel

The side propeller

The four-blade off-the-shelf propeller (Figure 3) has been chosen to mimic the Eurocopter X3 dimensions, thrust, and tip speed. The propeller, supplied by APC Propeller, is made of glass-filled nylon. A diameter of 0.28 m (11 inches) has been chosen to conserve the geometric propeller to main rotor diameter ratios between the model and the real configuration. The blade twist is 9° . The geometry of the blade has been provided by the supplier, and the 2D airfoil tables have been obtained using the elsA CFD software (Cambier and Veuillot 2008).

A tip cone has been set to obtain a smoother flow. A fairing has been designed to isolate the balance from the flow created by the propeller wake and the wind. A preliminary study on the isolated propeller proved the efficiency of these devices (Lefevre and Nowinski 2020). All the results presented in this article are measured at $\Omega_{prop} = 7500 \pm 30$ rpm.



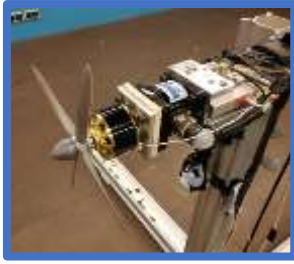


Figure 3 - Isolated small-scale propeller mounted in the L2 subsonic wind tunnel

L2 wind tunnel

This study has been conducted in the ONERA large size-low speed L2 wind tunnel (Figure 4). This open-circuit installation has been in operation since 1968 for naval, industrial, and aeronautical applications with a broad panel of measurement techniques. The test section measures 6 m x 2.4 m x 13 m.

The air circulation is carried out by eighteen fans divided into three horizontal lines and six columns. All together, the fans can generate a maximum velocity of 19 m/s in the test section. The flow then freely diffuses to the sides and top before returning to the entrance of the tunnel. Upstream to the test section inlet, the air flows through a honey comb to limit turbulence and to align the flow in the axial direction.

The wind tunnel operates at ambient atmospheric conditions. The humidity, ambient static pressure and temperature are measured in the undisturbed air in the hall. Since a maximum air density variation of 2 % has been calculated during the campaign, no correction has been applied. Considering the low velocities involved, the natural heat transfers only generates a 5°C per hour temperature increase in continuous operations at full power thanks to the air flow stream that ensures the cooling of the fans electric engines. Nevertheless, Pitot tubes are set in vein to monitor the evolution of the wind speed and prevent any variation during the measurements.

The turbulence profile shows values up to 7.6 % close to the walls, and less than 3 % in the middle of the

section. In this study, the blockage effect due to the test bench is small as it only covers 1.5 % of the wind tunnel test section.

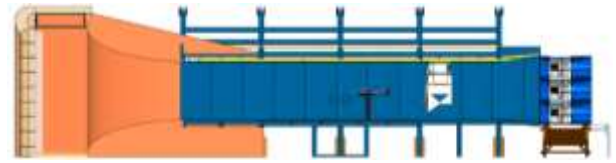


Figure 4 - Scheme of the INTROH bench mounted in the L2 subsonic wind tunnel

SPIV setup

Stereoscopic PIV measurements have been conducted. The air has been seeded with fine droplets of olive oil. With a density of 0.9137 g/cm³, the fluid has proven its ability to not disrupt the air flow while effectively reflecting light. Droplets with a diameter of 10 µm are created approximatively two meters upstream to the honeycomb, ensuring the homogeneity of the seeding in the test section.

Two acquisition planes are studied : one is placed upstream to the propeller, and the second downstream. The PIV planes measure 325 mm x 340 mm, with a resolution of one vector every 3 mm to 6 mm. For the upstream plane, the tip of the propeller cone is located at (-140 mm, -280 mm) in nominal position and at (0 mm, -280 mm) in backward position. For both positions, the PIV plane is placed just upstream of the propeller cone.

For the downstream plan, the study is conducted in the +1X position. In the downstream plane, the interference of the rotor blades with the cameras compromised the validity of the lower part of the image. Therefore, only the upper 150 mm will be analyzed in the article.

The Figure 5 suggests that the main rotor interfere in the measurement window, but the rotation leads to an elevation of the blades. Therefore no interference between the measurement window and the PIV plane is observed during the tests.

The coordinate system is defined such that \vec{U} is the velocity along \vec{x} and directed towards the tail of the aircraft, \vec{V} is the vertical velocity directed towards the rotor head, and \vec{W} the out-of-plane component defined such that a positive velocity is directed towards the left side of the helicopter from the pilots point of view. The in-plane norm of the velocity is calculated with $Norm = \sqrt{U^2 + V^2}$.

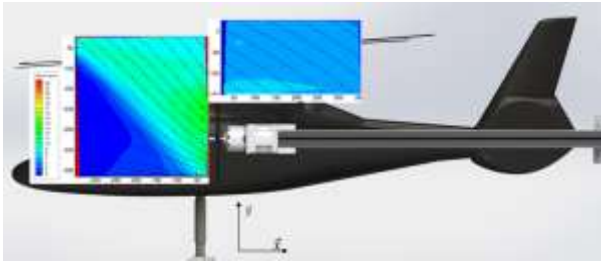


Figure 5 - Scheme of the PIV plane placement on the full assembly

The acquisition is performed with a laser and two high resolution cameras. The 2 x 400 mJ pulsed laser is activated at a wave length of 532 nm. The acquisition frequency is 5 Hz, which allows the decoupling of the PIV measurements with the rotor frequency (16.7 Hz) and to focus on the analysis on the rotor wake rather than blade passing unsteady effects. The pulse duration is of 5 ns.

The LaVision 4M cameras have a resolution of 2048 x 2048 pixels. The square pixels measure 7.4 μm x 7.4 μm , and the particles extend over 1.5 pixels. The time step is chosen for each wind speed to allow a typical particles displacement of 5 to 6 pixels between the two images. The spatial resolution of the interrogation windows is of 4.7 mm to 4.9 mm depending on the flight configuration. An overlapping of 70% of the interrogation windows is set. The cameras are positioned at a lateral distance of 2.1 m on the port side of the helicopter. The first camera is positioned at ground level, while the second is placed at 2.055 m height (Figure 6). The cameras cover an angle of about 50°.



Figure 6 - Implementation of the PIV setup in the L2 wind tunnel during calibration

The ONERA FOLKI software (Champagnat et al. 2011) is used to reconstruct the velocity fields based on a modified iterative wrapping similar to the dense Lukas-Kanade algorithm (Le Besnerais and Champagnat 2005). The window size is of 32 x 32 pixels². Most of the results that will be presented in the following are averages velocity maps over the 3000 instantaneous results obtained for each flow configuration.

Tests conducted

A parametric study has been conducted to analyze the influence of the propeller's position on the performances of the aircraft. During the campaign, the wind speed was varied from $U=5$ m/s to $U=19$ m/s, operating through all the L2 wind tunnel capabilities. Considering the rotational speed of the main rotor, this corresponds to advance ratios from $\mu = U/V_{tip} = 0.06$ to $\mu = 0.22$.

Velocity fields measurements were realized for two longitudinal positions. The nominal position is similar to what can be observed on the Eurocopter X3: the propeller is placed 0.14 m ahead of the rotor center (one propeller radius), at half a rotor radius laterally (0.375 m), and 0.28 m under the rotor head. The position +1X is obtained when moving the propeller of one propeller radius towards the tail of the helicopter, and aligning it with the rotor center.

The data are recorded for 10 minutes, allowing the acquisition of 3000 PIV maps per flight case. The images presented in this paper are averaged over the complete set. Averages are calculated by considering only the points with a cross correlation greater than 0.2, meaning that at least 20% of the particle are observed in both images. As more unsteadiness is observed on the downstream plane, the post-treatment criterion is set at 40 %. The 95 % confidence interval is under 0.1 m/s (less than 2 % of the lowest value of the wind speed) over the entire map (Figure 7).

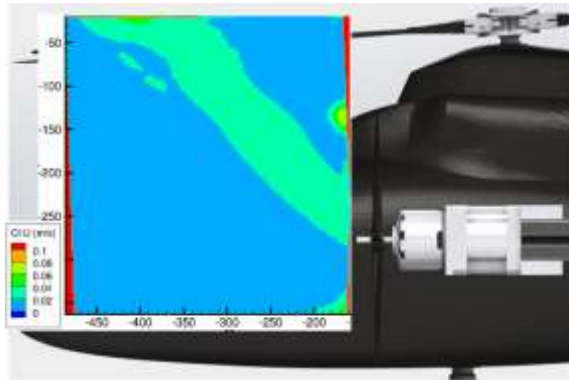


Figure 7 – 95 % confidence interval in nominal position at $\mu = 0.06$ (upstream plane)

During the entire campaign, three trim conditions are set : the thrust ($F_{z,rotor}$) is of 99.3 N, which corresponds to a dimensionless loading $\bar{z} = 14.5$. The thrust is set with an accuracy of ± 3 N. The longitudinal load ($F_{x,rotor}$) is adjusted to compensate the fuselage drag previously identified on the isolated helicopter [± 0.5 N]. To suppress the lateral effort ($F_{y,rotor}$), the longitudinal flap angle (β_{1s}) is zero [$\pm 0.5^\circ$].

Results

Hovering flight

Knowing that the droplet generator is placed upstream of the honeycomb, only the activation of the wind tunnel could ensure a homogeneous seeding in the test section. Therefore, no PIV measurements could be conducted for this flight configuration.

However, numerical studies conducted in the nominal position (Figure 8, (Boisard 2018; Boisard and Lim

2021; Boisard 2022)) showed that the rotor wake creates the equivalent of a 14 m/s flow impacting the propeller at a 90° angle. The propeller is therefore completely immersed in the rotor wake. Reciprocally, the propeller suction deflects the rotor wake to an angle of about 60° .

It can be predicted that the interactions would be similar in the position +1X, where the propeller is moved back by one propeller radius and placed at the center of the rotor wake.

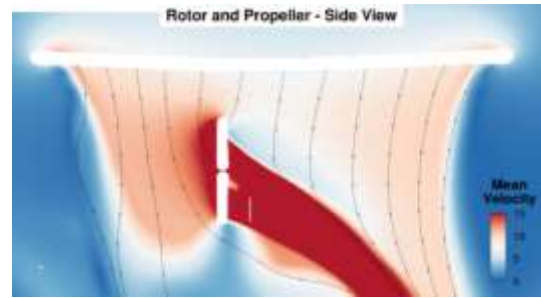


Figure 8 - Numerical estimation of the rotor wake development in hover (Boisard 2021)

Low speed flight

This section is focusing on the averaged velocity fields obtained at low flight speed ($\mu = 0.06$).

A study was first conducted at $\Omega_{prop} = 0$ rpm to present a base case, without the influence of the propeller on the flow (Figure 9). This study was performed in the +1X position, but similar conclusions could be drawn in the nominal position. This case can directly be compared to the results presented in Figure 10, where the propeller is rotating at $\Omega_{prop} = 7500$ rpm. Regardless of the propeller activation, the upstream flow evolves at 5 m/s. A slight acceleration of the free flow is measured up to 0.20 m ahead of the propeller when $\Omega_{prop} = 7500$ rpm (Figure 10)

On the other hand, while the rotor wake evolves at 45° when $\Omega_{prop} = 0$ rpm, it is straightened under the influence of the propeller suction and reaches an angle of about 30° at the rotor wake boundary just upstream of the propeller. The suction effect of the propeller on

the development of the rotor wake and on the free flow is therefore clearly highlighted.

The influence of the propeller is also underlined by the out of-plane velocity profile (Figure 9 and Figure 10-right). The flow norm and angle inside the rotor wake remain unchanged regardless of the propeller activation, but the rotor wake boundary is underlined when the propeller is activated. This highlights the influence of the rotation of the propeller blades on the free flow.

The Figure 10 and Figure 11 present the comparison of the flows between the nominal and the +1X positions at $\mu = 0.06$. The upper part of the rotor wake remains unchanged: the wake evolves at an angle of about 45° directed towards the upper part of the propeller.

In nominal position, the distance between the rotor wake front and the propeller is 0.14 m smaller. Therefore, when moved towards the tail of the helicopter, a larger part of the propeller disk is immersed in the rotor wake. Balance measurements (Lefevre et al. 2021) showed an increased propeller thrust, which can be explained by the larger angle of attack of the flow on most of the propeller disk

The off-plane velocity distribution is slightly different between the two configurations. While \vec{W} is of the same order under all over the wake boundary in the nominal position, a decrease is measured on the lower part of the image in the +1X position. This observation is caused by the stronger interaction between the rotating elements in the +1X position: the rotor wake is therefore realigned under the stronger influence of the propeller suction in backward position.

The off-plane velocity profile inside the rotor wake is however the same for both configurations, confirming the hypothesis that the propeller/rotor interactions are negligible for this configuration.

Finally, the results obtained downstream to the propeller (Figure 12) are presented for the nominal and +1X positions. The bottom left angle of the plane is placed at the crossing of the fairing with the propeller. Due to experimental limitations, only the upper part of the PIV plane is interpretable. This study highlights that the velocity of the rotor wake is similar under the entire rotor disk. The negligible influence of the propeller on the rotor is also underlined.

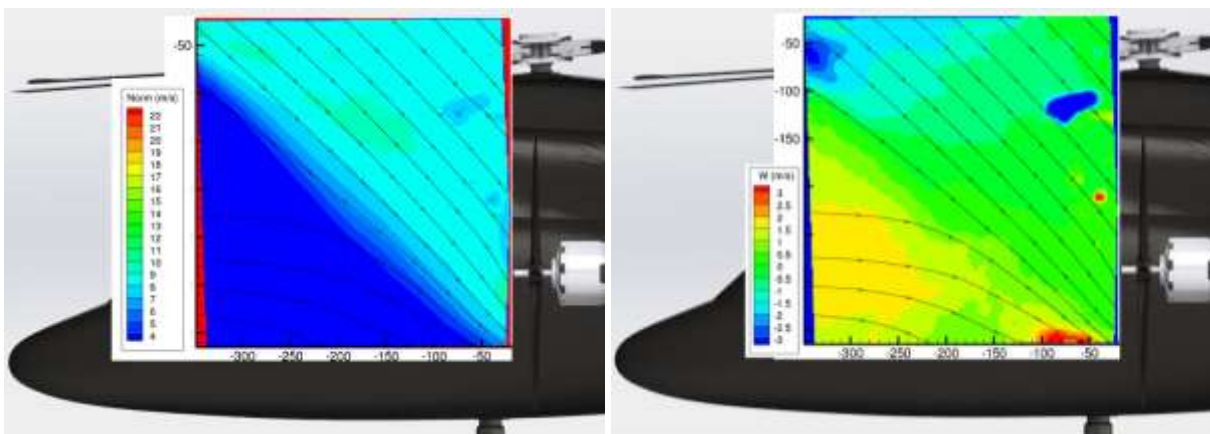


Figure 9 – Averaged 3D velocity field in +1X position at $\mu = 0.06$ and $\Omega_{prop} = 0$ rpm (upstream plane)

Norm of the in-plane velocity (left) and out of plane velocity W (right)

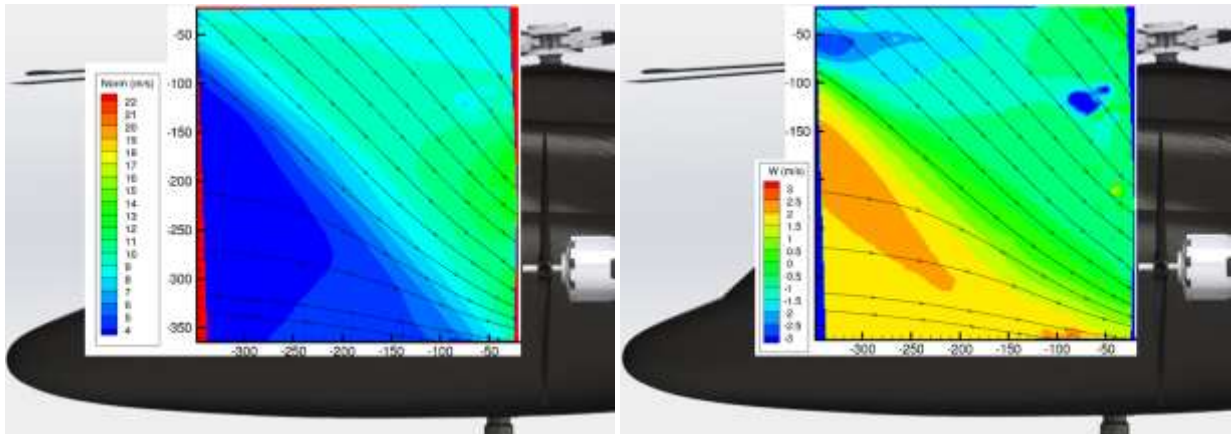


Figure 10 – Averaged 3D velocity field in +1X position at $\mu = 0.06$ (upstream plane).
 Norm of the in-plane velocity (left) and out of plane velocity W (right)

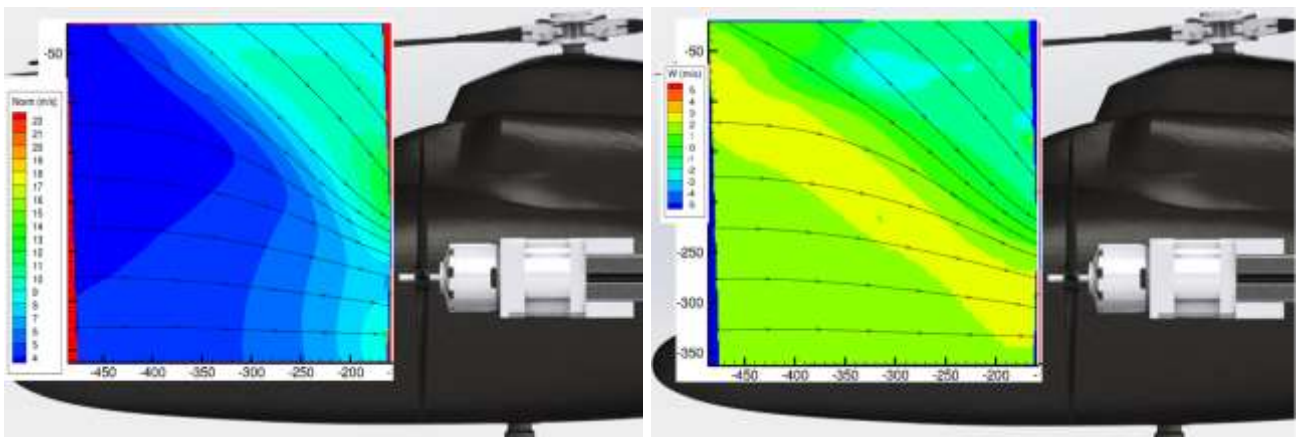


Figure 11 – Averaged 3D velocity field in nominal position at $\mu = 0.06$ (upstream plane).
 Norm of the in-plane velocity (left) and out of plane velocity W (right)

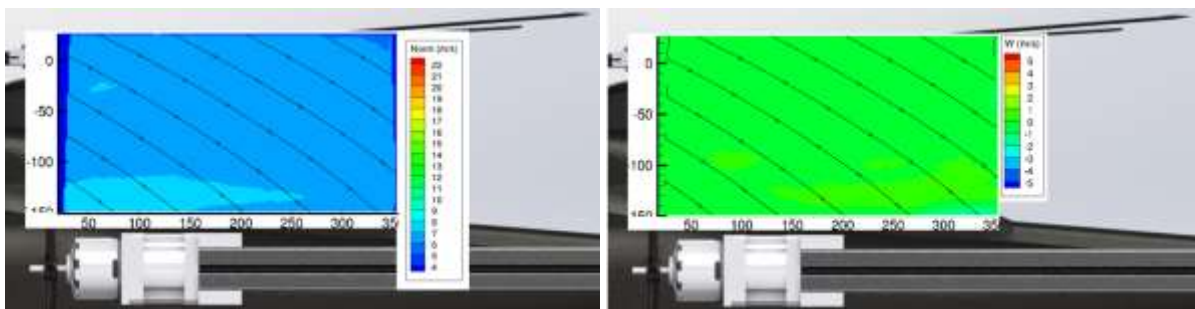


Figure 12 - Averaged 3D velocity field at $\mu = 0.06$ in +1X position (downstream plane).
 Norm of the in-plane velocity (left) and out of plane velocity W (right)

High speed flight

The results at high speed flight are presented in Figure 13 and Figure 14 for $\mu = 0.22$. At these operating conditions, the rotor wake passes well above the propeller: the flow is indeed sucked upstream of the rotor head. Since the PIV plane is translated between the two positions to follow the propeller, it is

highlighted that the velocity fields do not depend on the propeller position. The Figure 13 and Figure 14 thus demonstrate once again the negligible influence of the propeller on the rotor at high speeds.

For both positions, an important off-field velocity appears in the rotor wake. The limit of the negative off-plane velocity is highlighted in the +1X position, where

the propeller disk (placed at $x = 160$ mm) is aligned with the rotor center. It is supposed that the off-plane negative velocity is a consequence of the rotation direction of the rotor: the PIV plane being placed under the advancing side of the main rotor, the blades evolve from the front right to the back left. In this context, a sign change is expected at the rotor head. However, the blades lead-lag mobility leads to a slight lag, explaining why the negative velocity appears at $x = 80$ mm in the +1X position.

The propeller suction is also observed in the lower right corner, where an acceleration of about 5 % of the upstream velocity is measured. The suction affects the flow up to 0.3 m upstream of the propeller. Increasing

the advance ratio or moving the propeller towards the tail of the device leads to a more important influence of the propeller suction. As for the study at low speed, an in-plane velocity peak is also measured just under the propeller tip for all the tested configurations.

A study of the velocity field just downstream of the propeller is also conducted (Figure 15), where the boundary of the rotor wake is highlighted. Like for the study at $\mu = 0.06$, the velocity norm inside the rotor wake is similar over the entire observed window. Therefore, the propeller/rotor interaction is constant in this area, as underlined by the deviation of the streamlines.

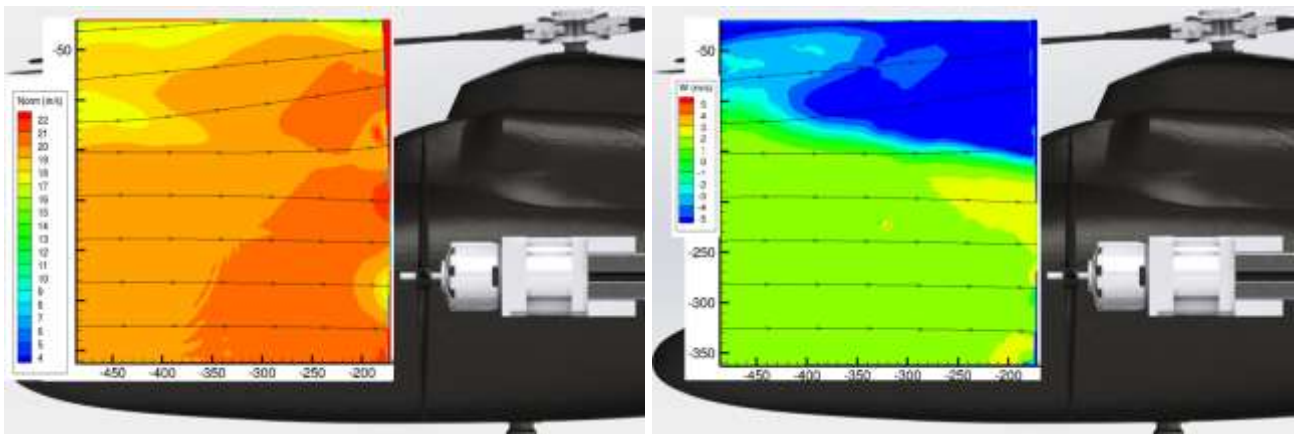


Figure 13 – In-plane norm (left) and out of-plane (right) velocity field at $\mu = 0.22$ in nominal position

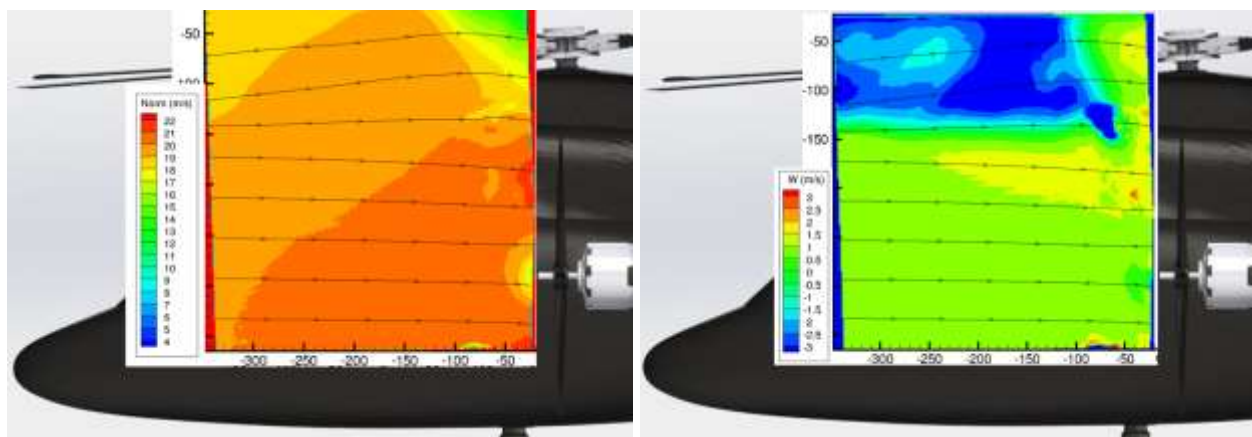


Figure 14- 3D velocity field at $\mu = 0.22$ in +1X position (upstream plane)

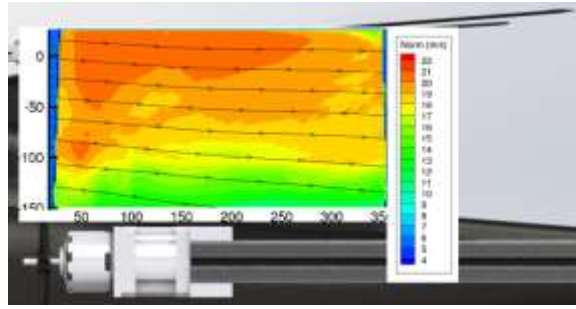


Figure 15 - 3D velocity field at $\mu = 0.22$ in +1X position (downstream plane)

Influence of the advance ratio

The Figure 16 and Figure 17 present the evolution of the in-plane velocity flow direction profile under the influence of the rotating elements for different advance ratios, and for two propeller positions. The flow angle is defined with $\alpha = \arctan(V/U)$. The profile are extracted at $x = 140$ mm, just upstream of the propeller.

For both propeller positions, increasing the advance ratio leads to a realignment of the flow. A clear change is observed between $\mu = 0.06$ and $\mu = 0.12$: this points out the limit between low and high speeds.

At low speed, the evolution of the flow is similar on the upper part of the window for both propeller positions. However, when the propeller is moved towards the tail of the rotor, a stronger acceleration and a more important flow angle are observed on the lower half of the plane. Indeed, the study at low speed highlighted that the rotor wake covers the majority of the height of the plane just upstream of the propeller in this position. The limit of the rotor wake is identified at $y = -120$ mm.

For both configurations, the propeller suction is measured at $y = -170$ mm.

At $\mu = 0.12$ the flow is slightly accelerated in the upper part of the image under the influence of the rotor wake for both propeller positions. The limit of the rotor wake is clearly visible at $y = 100$ mm for the nominal position and $y = 50$ mm when the propeller is pushed towards the tail of the rotor. For $\mu \geq 0.17$, a slight deceleration is observed on the upper part of the window under the influence of the rotor wake suction.

For all configurations with $\mu \geq 0.12$, the angle of the flow on the upper part of the interrogation window is slightly increased when the propeller is pushed towards the tail of the rotor. This is due to the more important distance between the front blade and the measurement plane, allowing the rotor wake to settle. The velocity profile is similar at high speed on the lower part of the window, only subject to the propeller suction. In both configurations, the absence of direct interactions between the rotors for $\mu \geq 0.12$ is underlined.

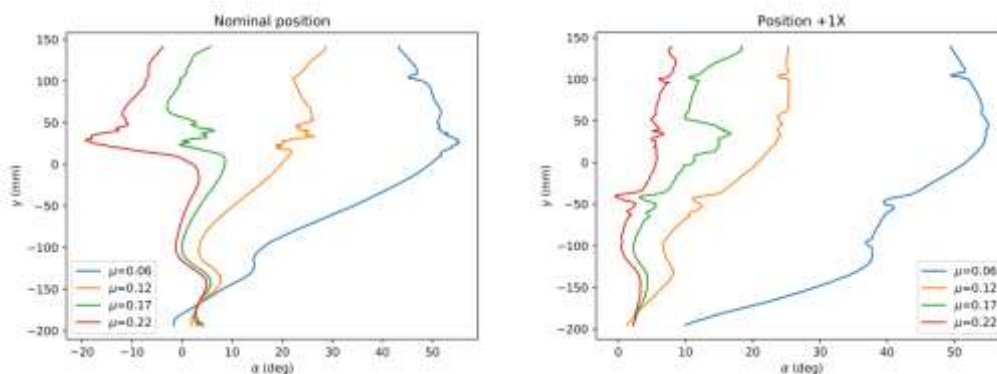


Figure 16 – Flow angle in nominal (top) and +1X (bottom) position for different advance ratios at $x = 140$ mm

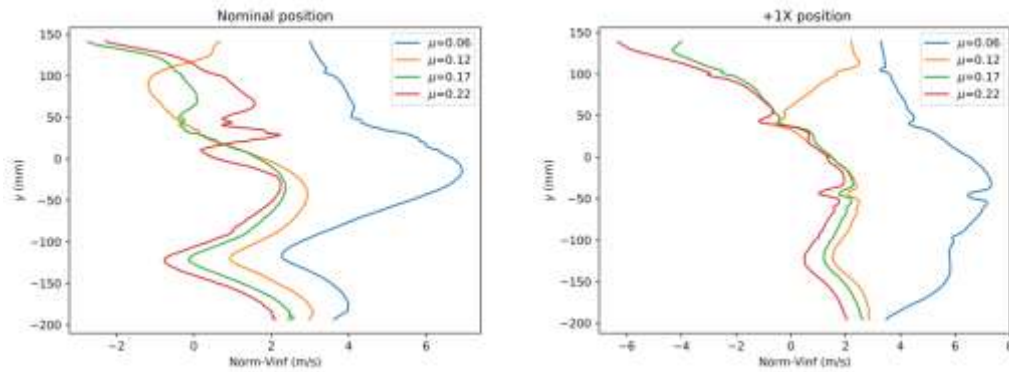


Figure 17 – Velocity profile in nominal (top) and +1X (bottom) position for different advance ratios at $x = 140$ mm

Conclusion

This study aimed to identify experimentally the influence of the propeller on the aerodynamic rotor/propeller interactions. Two configurations were tested: one mimicking the Eurocopter X3 where the propeller is placed 0.14 m upstream of the rotor center, and one where the propeller is pushed towards the tail of the helicopter and aligned with the rotor head.

In hover, the performances of the propeller are the same for the two configurations tested. The propeller is entirely immersed inside the rotor wake, and the interactions are not modified.

At high speed ($\mu \geq 0.12$), no direct interactions are observed. Moving the propeller towards the tail of the rotor therefore does not influence the interactions between the rotors.

At low speeds ($\mu = 0.06$), the propeller is partially immersed inside the rotor disk. Therefore, moving the propeller towards the tail of the device increases the rotor/propeller interactions, leading to increased propeller thrust.

For all flight configurations, the influence of the propeller on the rotor has been proven to be small. However, the influence of the propeller on the upstream flow is not negligible as it begets an acceleration and a deviation of the flow.

Declarations

Consent for publication: The authors confirm that this work is original and has not been published elsewhere, nor is it under consideration for publication elsewhere, and consent for the publication in Experiments in Fluids.

Availability of data and material: The data that support the findings of this study are available from the corresponding author, upon reasonable request.

Competing interests: The authors declare that they have no known competing financial interests or personal relationships that could have appeared to influence the work reported in this paper.

Authors contributions: Lauriane Lefevre (corresponding author) - Tests, writing, reviewing and editing. Vianney Nowinski - Supervision, tests, reviewing. Jérôme Delva - Tests and reviewing. Antoine Dazin - Reviewing. All authors approved the version to be published

Funding: The authors gratefully acknowledge the financial support given by ONERA and the Région Hauts-de-France.

Acknowledgements: The technical support of Ronan Boisard and François Richez for the numerical study is thanked.

Ethics approval and consent to participate: not applicable

References

- Boisard, Ronan. 2018. "Aerodynamic Investigation of Rotor/Propeller Interactions on a Fast Rotorcraft", In *44th European Rotorcraft Forum*, Delft, The Netherlands.
- . 2021. "Numerical Analysis of Rotor/Propeller Aerodynamic Interactions on a High-Speed Compound Helicopter," In *77th Vertical Flight Society Forum*.
- . 2022. "Numerical Analysis of Rotor/Propeller Aerodynamic Interactions on a High-Speed Compound Helicopter." *Journal of the American Helicopter Society* 67 (1): 1–15.
- Boisard, Ronan, and J. W. Lim. 2021. "Aerodynamic Analysis of Rotor/Propeller Wakes Interactions on High Speed Compound Helicopter." In *47th European Rotorcraft Forum*.
- Cambier, Laurent, and Jean-Pierre Veuillot. 2008. "Status of the ElsA Software for Flow Simulation and Multi-Disciplinary Applications." In *46th AIAA Aerospace Sciences Meeting and Exhibit*. American Institute of Aeronautics and Astronautics..
- Champagnat, F., A. Plyer, G. Le Besnerais, B. Leclaire, S. Davoust, and Y. Le Sant. 2011. "Fast and Accurate PIV Computation Using Highly Parallel Iterative Correlation Maximization." *Experiments in Fluids* 50 (4): 1169..
- Ferguson, K., and D. Thomson. 2015. "Performance Comparison between a Conventional Helicopter and Compound Helicopter Configurations." *Journal of Aerospace Engineering*, Part G, 229 (13): 2441–56..
- Floros, Matthew, and Wayne Johnson. 2009. "Performance Analysis of the Slowed-Rotor Compound Helicopter Configuration." *Journal of the American Helicopter Society*, Vertical Flight Society, 54 (2): 22002..
- Le Besnerais, G., and F. Champagnat. 2005. "Dense Optical Flow by Iterative Local Window Registration." In *IEEE International Conference on Image Processing 2005*, 1:1–137.
- Le Pape A., Gatard J., and Monnier J.-C. 2007. "Experimental Investigation of Rotor-Fuselage Aerodynamic Interactions." *Journal of the American Helicopter Society*, Vertical Flight Society, 52 (2): 99.
- Lefevre, Lauriane, and Vianney Nowinski. 2020. "Characterization of the Propeller for the Experimental Evaluation of the Aerodynamic Rotor/Propeller Interactions in Hybrid Compound Helicopters." In *ONERA-DLR Annual Symposium*.
- Lefevre, Lauriane, Vianney Nowinski, Jérôme Delva, and Antoine Dazin. 2021. "Experimental Evaluation of the Aerodynamic Rotor/Propeller Interactions in Hybrid Compound Helicopters." In *47th European Rotorcraft Forum*.
- . 2022. "Experimental Evaluation of the Aerodynamic Rotor/Propeller Interactions on High Speed Helicopters, Efforts and Velocity Fields Measurements." In *78th Vertical flight Society Forum*, Fort Worth, Tx.
- Lorber, Peter, Gary Law, John O'Neill, Sikorsky Aircraft, Claude Matalanis, Patrick Bowles, and United Technologies Research Center. 2016. "Overview of S-97 RAIDER Scale Model Tests." In *72nd AHS International Forum*, West Palm Beach, Florida.
- Öhrle, Constantin, Felix Frey, Jakob Thiemeier, Manuel Keßler, Ewald Krämer, Martin Embacher, Paul Cranga, and Paul Eglin. 2021. "Compound Helicopter X 3 in High-Speed Flight: Correlation of Simulation and Flight Test." *Journal of the American Helicopter Society* 66 (1).
- Orchard, M, and S Newman. 2003. "The Fundamental Configuration and Design of the Compound Helicopter." *Journal of Aerospace Engineering*, Part G, 217 (6): 297–315.
- Rand, Omri, and Vladimir Khromov. 2015. "Compound Helicopter: Insight and Optimization." *Journal of the American Helicopter Society*, *AHS 69th Annual Forum*, Phoenix, USA
- Renaud, Thomas, Marilyn Smith, Mark Potsdam, and David O'Brien. 2008. "Evaluation of Isolated Fuselage and Rotor-Fuselage Interaction Using Computational Fluid Dynamics." *Journal of the American Helicopter Society*, Vertical Flight Society, 53 (1): 3–17.
- Russell, Carl M., and Wayne Johnson. 2012. "Conceptual Design and Performance Analysis for a Large Civil Compound Helicopter." In *AHS Vertical Lift Aircraft Design Conference*, San Francisco, CA.
- Stokkermans, T. C. A. 2020. "Aerodynamics of Propellers in Interaction Dominated Flowfields." *PhD thesis*, Delft, The Netherlands: TU Delft.
- Thiemeier, Jakob, Constantin Öhrle, Felix Frey, Manuel Keßler, and Ewald Krämer. 2019. "Aerodynamics and Flight Mechanics Analysis of Airbus Helicopters' Compound Helicopter RACER in Hover under Crosswind Conditions." *CEAS Aeronautical Journal*, April.
- Wieneke, Bernhard. 2015. "PIV Uncertainty Quantification from Correlation Statistics." *Measurements Science and Technology*, 26-7.
- Yeo, Hyeonsoo, and Wayne Johnson. 2007. "Aeromechanics Analysis of a Heavy Lift Slowed-Rotor Compound Helicopter." *Journal of Aircraft* 44 (2): 501–8.